



Modeling of salt and gypsum dissolution: applications, evaluation of geomechanical hazards

Farid Laouafa, Jianwei Guo, Michel Quintard

► To cite this version:

Farid Laouafa, Jianwei Guo, Michel Quintard. Modeling of salt and gypsum dissolution: applications, evaluation of geomechanical hazards. *European Journal of Environmental and Civil Engineering*, 2021, 25 (8), pp.1405-1426. 10.1080/19648189.2019.1579758 . hal-02134740

HAL Id: hal-02134740

<https://hal.science/hal-02134740>

Submitted on 20 May 2019

HAL is a multi-disciplinary open access archive for the deposit and dissemination of scientific research documents, whether they are published or not. The documents may come from teaching and research institutions in France or abroad, or from public or private research centers.

L'archive ouverte pluridisciplinaire **HAL**, est destinée au dépôt et à la diffusion de documents scientifiques de niveau recherche, publiés ou non, émanant des établissements d'enseignement et de recherche français ou étrangers, des laboratoires publics ou privés.




Open Archive Toulouse Archive Ouverte (OATAO)

OATAO is an open access repository that collects the work of some Toulouse researchers and makes it freely available over the web where possible.

This is an author's version published in: <https://oatao.univ-toulouse.fr/23760>

Official URL : <https://doi.org/10.1080/19648189.2019.1579758>

To cite this version :

Laouafa, Farid and Guo, Jianwei and Quintard, Michel  *Modeling of salt and gypsum dissolution: applications, evaluation of geomechanical hazards.* (2019) European Journal of Environmental and Civil Engineering. 1-22. ISSN 1964-8189

Any correspondence concerning this service should be sent to the repository administrator:
tech-oatao@listes-diff.inp-toulouse.fr

Modeling of salt and gypsum dissolution: applications, evaluation of geomechanical hazards

Farid Laouafa^a, Jianwei Guo^b and Michel Quintard^c

^aInstitut National de l'Environnement Industriel et des Risques-INERIS (France), Verneuil-en-Halatte, France;

^bSchool of Mechanics and Engineering, Southwest Jiaotong University, Chengdu, China; ^cInstitut de Mécanique des Fluides de Toulouse (IMFT), Université de Toulouse, CNRS, Toulouse, France

ABSTRACT

This article addresses the problem of modeling the dissolution of cavities in gypsum and halite (salt), followed by the assessment of potential collapse or subsidence of the geological formation, which may induce damaging consequences for population and infrastructures. Hazard prediction relies mostly on numerical modeling. This article discusses several issues associated to the development of dissolution numerical models involving the coupling between transport, dissolution and geomechanical modeling: type of model, parameters and numerical strategies. Hazard prediction relies mostly on numerical modeling. This article discusses several issues associated to the development of dissolution numerical models involving the coupling between transport, dissolution and geomechanical modeling: type of model, parameters and numerical strategies. The methodology is illustrated on several boundary value problems typical of actual situations in mining or civil engineering.

KEYWORDS

Dissolution; diffuse interface method; gypsum; salt; geomechanics; modeling

1. Introduction

The dissolution of evaporites, such as salt and gypsum deposits, is a problem widely encountered in natural processes and engineering applications (Waltman et al., 2005). As important bed-rocks of karstic structures, salt and gypsum are about 7500 and 150 times more soluble than limestone, respectively (de Waele et al., 2017; Martinez, Johnson, & Neal, 1998; Waltham, Bell, & Culshaw, 2005). Although we are interested in dissolution of soluble rocks, the work presented in this article has a much wider field of application: ablation of solid-composite materials, acid injection into petroleum reservoirs, industrial process, optimisation in salt extraction for example, by the so call 'solution mining' method, analysis of pollution induced by dissolution and the transport of brine in aquifers, etc. Geohazards, such as subsidence and collapse of sinkholes (Gutierrez, Parise, De Waele, & Jourde, 2014; Waltham et al., 2005), which are often related to the evolution of underground cavities, may form in a relatively short time in the case of evaporite dissolution. Figure 1 presents an example of the catastrophic results induced by salt dissolution. This emphasizes the importance of having a better understanding such dissolution of underground cavities in order to predict the occurrence of such disasters and take safety measures. It is also important to notice that a better knowledge of subsurface dissolution is also beneficial to



Figure 1. Land subsidence in Central Kansas related to salt dissolution (Walters, 1978).

many industrial applications, such as, for instance: the optimisation of inlet flux in solution mining and improved oil recovery, and the assessment of long-term integrity of caprock in CO₂ geological storage.

Natural geological systems are often highly heterogeneous, involving multiple scales ranging from pore-scale of millimeter size, to large-scale of tens of meters (Guo, Quintard, & Laouafa, 2015; Guo, Laouafa, & Quintard, 2016), as schematically illustrated in Figure 2. Consequently, the numerical simulation of subsurface dissolution of porous media or cavities can be conducted at different scales. If one is interested in the pore-scale behaviour, then pore-scale modeling is the most secure way because it makes the minimum approximations with the advantage of considering explicitly the solid geometry, provided the required number of DOFs (degrees of freedom) is not too large for computational purposes. The recession of the solid grains is determined by a pore-scale transport problem including the surface reaction rate in the boundary condition for the solid–pore interface. The reaction rate for such materials is often expressed as (Jeschke & Dreybrodt, 2002; Jeschke, Vosbeck, & Dreybrodt, 2001):

$$R = k \left(1 - \frac{C}{C_{eq}} \right)^n \quad (1)$$

for carbonate rocks (e.g. limestone and calcite) and gypsum. Here, k is the surface reaction rate coefficient, C is the mass concentration of the dissolved species at the surface, and C_{eq} is the equilibrium concentration or solubility. However, for the dissolution of salt, a very large value of k makes the boundary condition close to the thermodynamic equilibrium condition

$$C = C_{eq} \quad (2)$$

at the solid surface.

Various techniques are available in the literature to solve the reactive transport problem at the pore-scale. A good representative is the Arbitrary-Lagrangian–Eulerian (ALE) technique, which describes the full dissolution physics and tracks the evolving solid–liquid interface explicitly with a deforming mesh (Donea, Giuliani, & Halleux, 1982; Luo, Quintard, Debenest, & Laouafa, 2012; Oltéan, Golfier, & Buès, 2013; Soulaine, Roman, Kovscek, & Tchelepi, 2017). The governing equations describing mass and momentum conservation are solved with high accuracy because all the pore-scale details are taken into account. However, re-meshing process is required to treat the topological changes and this limits the application of ALE within a few grains. Therefore, it is not practical to implement direct numerical modeling with ALE to describe large-scale problems with numerous grains. However, ALE is a good reference method to verify the accuracy of other approaches (Luo et al., 2012; Luo, Laouafa, Guo, & Quintard, 2014; Soulaine et al., 2017). Compared to the front-tracking methods which express the interface explicitly, the front capturing methods such as the Level Set approach follow the interface implicitly (Osher & Fedkiw, 2001; Sethian & Smereka, 2003). The interface in Level Set method is captured by a level set

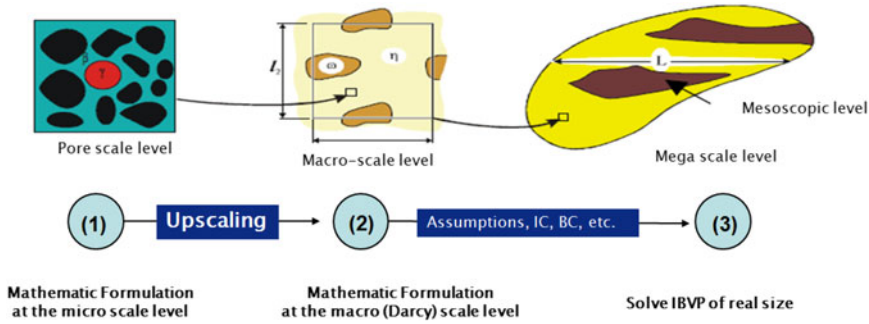


Figure 2. From micro scale to large scale levels.

function represented by a smeared Heaviside function. The level set function changes smoothly across the interface from 0 to 1 and the interface is represented by the 0.5 isocontour of the level set function. The mass conservation and convergence problems of early level set method have been overcome by modifying the advection of interface and the reinitialisation step (Olsson, Kreiss, & Zahednia, 2007). Alternative pore-scale methods include the pore network models (PNM) (Alghamdi, Békri, Nader, Lerat, & Vizika, 2012; Békri, Renard, & Delprat-Jannaud, 2015; Chen, Kang, Carey, & Tao, 2014; Nogues, Fitts, Celia, & Peters, 2013; Sun, 2012; Varloteaux, Vu, Békri, & Adler, 2013; Varloteaux, Békri, & Adler, 2013). In PNM, the pore-scale geometry is transformed into a network of pore bodies connected by pore throats. Flow dynamics in the system is resolved by using approximations such as Poiseuille flows for the momentum balance. Such a conceptual representation of the porous medium considers the topological effects, such as the connectivity, the aspect ratio and tortuosity, etc. (De Boever et al., 2012). It is able to approximately reproduce the pore-scale dissolution process to a certain accuracy and thus solve for much larger volumes, i.e. including a larger number of pores (Varloteaux, Vu, et al., 2013). Recently, the lattice Boltzmann method (LBM) (Chen et al., 2014; Huber, Shafei, & Parmigiani, 2014; Kang, Zhang, Chen, & He, 2002; Kang, Chen, Valocchi, & Viswanathan, 2014; Szymczak & Ladd, 2004) is also widely used. While valuable information is obtained from these pore-scale simulations, it is not convenient to use them in a macro-scale problem due to several constraints. Firstly, the computational cost when dealing with large-scale problems, such as cavity evolution and solution salt mining, is too expensive. Secondly, the explicit tracking of the moving interfaces in some circumstances induces numerical difficulties due to the large deformation of the configuration. Thirdly, the pore-scale details of the medium under investigation are often difficult to obtain and may not be of practical interest. As a matter of fact, one would be more interested in a macro-scale description of the dissolution problem in engineering practice. Therefore, macro-scale models may be developed to filter the pore-scale details and predict only their averaged behaviours.

The development of various macro-scale models is dependent on the problem involved. For example, when the dissolution of solid formations with heterogeneous, rough surface is concerned, the effective surface theory may be implemented to find a homogeneous, smooth surface with effective boundary conditions representing the average displacement of the rough surface. When modeling reactive flow in porous media, upscaling through various techniques, such as the method of volume averaging (Whitaker, 1999), the method of moment (Brenner & Stewartson, 1980) or the method of homogenisation (Mauri, 1991), etc., can be implemented to upscale the pore-scale models into macroscopic ones. Several important effective parameters may be introduced in the macro-scale models to link the averaged behaviour with the pore-scale features, and they are obtained by solving the so-called closure problems developed in the upscaling process. Among various effective parameters, the effective dispersion tensor (Guo et al., 2015; Jourak, Hellström, Lundström, & Frishfelds, 2014; Luo et al., 2012, 2014) and the

effective mass exchange coefficient (Coutelieris, Kainourgiakis, Stubos, Kikkinides, & Yortsos, 2006; Guo et al., 2015, 2016) are of great significance. In addition, non-classical parameters may also have some influences on the accuracy of the macro-scale models, as discussed in Guo et al. (2015). Darcy-scale non-equilibrium models have been successfully used in Guo et al. (2016), Soulaine et al. (2017), Zhao, Hobbs, Ord, and Peng (2010) to describe the moving front between fluid and porous domains, with the front represented by a transient zone characterised by a porosity gradient.

The above mentioned local non-equilibrium models developed for the dissolution of porous media may also be used as diffuse interface models (DIM) for describing the dissolution of a pure solid. DIM has the advantage of not following the solid–liquid interface explicitly. Consequently, it can be used to solve problems with rather complicated geometry. A smoothly varying phase indicator, such as the porosity or concentration of the dissolved species, can be used to indicate the dissolution front. When the effective mass exchange coefficient is large enough, the front tends to be very thin and local equilibrium condition is recovered. The ability of DIM to capture the recession of solid formations, even coupled with hydrodynamic instabilities such as natural convection, has been demonstrated in several works (Luo et al., 2012, 2014; Guo et al., 2016).

In this article, we are interested in the potential to use DIM in conditions corresponding to real industrial situations. Since the framework to develop the volume averaged equations and to use them for the modeling of given soluble rocks has been provided in several previous works (Guo et al., 2015, 2016; Luo et al., 2014), this question will not be detailed in the article which is organised as follows. We will first go briefly through the theoretical part for reader's comprehension. Then, the emphasis will be put on some applications of DIM to solve problems of metric scale with large singularity and strong natural convection effects. Finally, geomechanical calculations will be performed on the resulting dissolved cavities to assess the potential for mechanical damage of the formation. The purpose of this article is to present an approach that can describe the dissolution of solids. This is the central element of this article. The theoretical examples treated and materials analysed (salt, gypsum), are given only for illustration and applicability purposes. The fields of application of the DIM method are very much broader.

2. Mathematical-physical problems

In this section, we first introduce a generic pore-scale dissolution model corresponding to dissolution of a soluble solid species considered as a single component. The approach can be extended to a material having several components (multi-components). In this case, the conservation equations apply to each component. Then brief indications will be given about the upscaling of the pore-scale equations to derive a macro-scale diffuse interface model, which can be used later to describe the dissolution of large cavities or porous media formations. This methodology is applicable for salt, gypsum and even carbonate rocks, provided local conditions are compatible with the assumption of a pseudo-component. Otherwise, the same methodology must be extended to a multicomponent treatment, which is beyond the scope of this article.

2.1 Pore-scale models

The introduction of a pseudo-component dissolving species is discussed in Guo et al. (2015) and Guo et al. (2016) for the case of gypsum. Several constraints must be satisfied. In particular, even if other dissolving compounds involving the same ions are present, the common-ion effect favors the dissolving material (like gypsum for instance) because of its strongest solubility. Secondly, individual species diffusion coefficient are similar, thus preventing segregation of ions in the solution. Thirdly, the physical properties such as density, viscosity and diffusion coefficients are

nearly uniform over a pore during the dissolution process. Such conditions are often satisfied for salt dissolution. This is also often acceptable for carbonate dissolution, provided thermodynamic conditions are nearly constant. Studies are performed under isothermal conditions.

The pore-scale solid/liquid dissolution problem can be described by classical convective–diffusive mass balances and Navier–Stokes (momentum) equations. The chemical reactions are incorporated in the corresponding boundary conditions at the liquid–solid interface. The solid and liquid phases (dissolving material and water in this study) are denoted as s and l , respectively. With the assumptions discussed above, mass balance equations for the incompressible liquid phase and the dissolved species can be written as:

$$\frac{\partial \rho_l}{\partial t} + \nabla \cdot (\rho_l \mathbf{v}_l) = 0 \quad \text{in the } l\text{-phase} \quad (3)$$

$$\rho_l \frac{\partial \omega_l}{\partial t} + \rho_l \mathbf{v}_l \cdot \nabla \omega_l = \nabla \cdot (\rho_l D_l \nabla \omega_l) \quad \text{in the } l\text{-phase} \quad (4)$$

with $\mathbf{v}_l(\mathbf{x}, t) \in \mathbb{R}^n$ the pore-scale liquid velocity, $\omega_l(\mathbf{x}, t)$ the mass fraction (mass of the chemical species divided by the mass of the liquid) of the pseudo-component in the liquid phase and $D_l(\mathbf{x}, t)$ the molecular diffusion coefficient. For the sake of clarity, we will note all the scalar, vectorial or tensorial variables field by omitting their function of space (\mathbf{x}) and time (t).

The boundary conditions for the pseudo-component mass balance at the solid–liquid interface (of outward normal \mathbf{n}_{ls}) may be written as a kinetic condition:

$$\mathbf{n}_{ls} \cdot (\rho_l \omega_l (\mathbf{v}_l - \mathbf{w}_{sl}) - \rho_l D_l \nabla \omega_l) = -M k_s \left(1 - \frac{\omega_l}{\omega_{eq}} \right)^n = \mathbf{n}_{ls} \cdot (-\rho_s \mathbf{w}_{sl}) \quad \text{at } A_{ls} \quad (5)$$

where ρ_l and ρ_s are the density of the liquid and the solid, respectively, \mathbf{w}_{sl} is the interface velocity, M is the molar weight of the pseudo-component, k_s is the reaction rate coefficient, n is the nonlinear reaction order, ω_s is the mass fraction of the pseudo-component in the solid phase and A_{ls} is the interfacial area between the solid and the liquid phase.

This equation can be used to calculate the *interface velocity*. It is important to remark that in general we have the following inequality

$$\|\mathbf{w}_{sl}\| \ll \|\mathbf{v}_l\| \quad (6)$$

For gypsum, for instance, the maximum value given by Equation (5) for $|\mathbf{n}_{ls} \cdot \mathbf{w}_{sl}|$ is about 9.7×10^{-8} m/s, which is negligible compared to seepage velocities in hydrogeology, on the order of 10^{-5} to 10^{-6} m/s.

Navier–Stokes equations are used to describe the momentum balance in the fluid phase, which can be written as:

$$\rho_l \frac{\partial \mathbf{v}_l}{\partial t} + \rho_l \mathbf{v}_l \cdot \nabla \mathbf{v}_l = -\nabla p_l + \rho_l \mathbf{g} + \mu_l \nabla^2 \mathbf{v}_l \quad \text{in the } l\text{-phase} \quad (7)$$

with \mathbf{g} the gravity and μ_l the dynamic viscosity. A boundary condition corresponding to no jump in the tangential velocity has to be enforced at A_{ls} .

Considering the generally very small convected normal mass flux at the solid–liquid interface, we can simplify Equation (5) into

$$\mathbf{n}_{ls} \cdot (-\rho_l D_l \nabla \omega_l) \approx -M k_s \left(1 - \frac{\omega_l}{\omega_{eq}} \right)^n \quad \text{at } A_{ls} \quad (8)$$

The recession velocity \mathbf{w}_{sl} can also be expressed as follows (Luo et al., 2012):

$$\mathbf{n}_{ls} \cdot \mathbf{w}_{sl} = \frac{\rho_l}{\rho_s} \frac{1}{(1 - \omega_l)} D_l \mathbf{n}_{ls} \cdot \nabla \omega_l \quad (9)$$

In the next section, we briefly describe the macroscopic (Darcy-scale) equations obtained by upscaling the set of pore-scale equations. The reader will find in Appendix the details of this change of scale problem.

2.2. Upscaling to the diffuse interface model

The method of volume averaging (Whitaker, 1999) has been used to average the pore-scale variables over a representative elementary volume (REV) as shown in Figure 2, based on the assumption of scale separation. The general framework of upscaling through the method of volume averaging has been developed for several decades and we refer the reader to the cited references for more information. The main steps to derive the Darcy-scale equations can be found in the above-cited references and we only present the closed form of the diffuse interface model (DIM) here. The mass transport equations can be written as

$$\frac{\partial(\varepsilon_s \rho_s)}{\partial t} = K_g \quad (10)$$

$$\frac{\partial(\rho_l \varepsilon_l)}{\partial t} + \nabla \cdot (\rho_l \mathbf{V}_l) = -K_g \quad (11)$$

$$\frac{\partial(\rho_l \Omega_l \varepsilon_l)}{\partial t} + \nabla \cdot (\rho_l \Omega_l \mathbf{V}_l) = \nabla \cdot (\varepsilon_l \rho_l \mathbf{D}_l \cdot \nabla \Omega_l) - K_g \quad (12)$$

where ε_s denotes the volume fraction of the solid, K_g the mass exchange of the dissolving species, ε_l the porosity (such that $\varepsilon_s + \varepsilon_l = 1$), \mathbf{V}_l the superficial average of the velocity (Darcy or superficial velocity), Ω_l the intrinsic average of the mass fraction of the dissolving species and \mathbf{D}_l the dispersion tensor. Detailed expressions for the last two terms can be found in Appendix and they can be obtained by solving closure problems developed in the upscaling process. However, instead of solving the closure problems for specific unit cells, the linear dispersion model

$$\mathbf{D}_l = \frac{D_l}{\tau_l} \mathbf{I} + \alpha_T \frac{\|\mathbf{V}_l\|}{\varepsilon_l} \mathbf{I} + (\alpha_L - \alpha_T) \frac{\mathbf{V}_l \mathbf{V}_l}{\|\mathbf{V}_l\| \varepsilon_l} \quad (13)$$

is often used, where the tortuosity, τ_l , the longitudinal, α_L and transversal, α_T , dispersivities depend on the pore-scale geometry. The mass exchange term K_g is often estimated in the literature as a first-order expression in terms of the mass fraction difference, i.e. $K_g = \rho_l \alpha (\Omega_l - \omega_{eq})$ where ω_{eq} is the mass fraction at equilibrium.

Regarding the momentum equations, we use a modified version of the Navier–Stokes equation in the dissolved region reminiscent of the Darcy–Brinkman equation:

$$\rho_l \frac{\partial \mathbf{V}_l}{\partial t} + \rho_l \mathbf{V}_l \cdot \nabla \mathbf{V}_l = -(\nabla P_l - \rho_l \mathbf{g}) + \mu_l \nabla^2 \mathbf{V}_l - \mu_l \mathbf{K}_l^{-1} \cdot \mathbf{V}_l \quad (14)$$

Here, a homogeneous μ_l instead of the so-called effective viscosity is practical for simplification, even though it may be heterogeneous due to the large spatial variations of material properties within the domain. Comparing to the use of different equations in separate domains, such as Navier–Stokes equation in the fluid zone and Darcy’s law in the porous domain, using Equation (14) has the following advantage. If local Reynolds number in the porous medium is small, which is the case in this present study, the inertia effects are negligible, and Equation (14) turns out to be the Darcy–Brinkman equation

$$-(\nabla P_l - \rho_l \mathbf{g}) + \mu_l \nabla^2 \mathbf{V}_l - \mu_l \mathbf{K}_l^{-1} \cdot \mathbf{V}_l = 0 \quad (15)$$

In the domain characterised with infinite (large enough) permeability, it simplifies to Stokes equation, i.e.

$$-(\nabla P_l - \rho_l \mathbf{g}) + \mu_l \nabla^2 \mathbf{V}_l = 0 \quad (16)$$

In contrary, Darcy's equation

$$\mathbf{V}_I = -\frac{\mathbf{K}_I}{\mu_I} \cdot (\nabla P_I - \rho_I \mathbf{g}) \quad (17)$$

is recovered if the permeability is small enough, which is the case for the application to bedrocks.

The exchange term in the reactive case can be written as;

$$K_g = -a_{vI} M \left(1 - \frac{\Omega_I}{\omega_{eq}} \right)^n k_{s,eff} + \dots \quad (18)$$

with $k_{s,eff}$ the macro-scale effective reaction rate coefficient. If a thermodynamic equilibrium condition $\omega_I = \omega_{eq}$ is prescribed (this is also obtained if the Damkhöller number defined as $Da = \frac{M}{\rho_I \omega_{eq}} \frac{L_r}{D_I} k_s \left(1 - \frac{\Omega_I}{\omega_{eq}} \right)^{n-1}$ is large, where L_r is a characteristic pore-scale length), the corresponding mass exchange term can be rewritten; as

$$K_g(1 - \omega_{eq}) = \rho_I \alpha_I (\Omega_I - \omega_{eq}) + \dots \quad (19)$$

with α_I the effective mass exchange coefficient.

The properties of the resulting model are the following:

- the dissolution front thickness is controlled through the effective mass exchange term, i.e. through α_I in the case of a thermodynamic equilibrium condition,
- if α_I is taken large-enough in the case of a thermodynamic equilibrium condition, the front thickness tends to zero and the model is equivalent to a pore-scale dissolution model. Hence, it can be used to model original solid dissolution problems or typical porous media dissolution problems.

The use of this model as a diffuse interface model to compute cavity formation has been discussed in general in Guo et al. (2016). Here, we demonstrate the applicability to real industrial configurations, and use the resulting cavity formations to perform geomechanical studies and estimate the potential for formation damage.

3. Numerical modeling of cavity formation

The purpose of this section is to illustrate the possibilities of the dissolution model that is presented Section 2.

First, we discuss in this section the creation of cavity by the so called direct and reverse injection methods. Gypsum or salt, will be considered. The same geometry (domain) and hydraulic boundary conditions are used for both materials. In the next section, we study the dissolution of a gypsum lens located in a porous domain and the dissolution of a pillar in a gypsum quarry flooded with a slow but permanent flow. For these two last examples, we analyse the mechanical effects of dissolution: surface subsidence in the case of the gypsum lens and stability in the case of the pillar.

This section is devoted to the numerical modeling of an experimental middle scale dissolution process. The goal is to show the ability of the DIM model to tackle difficult problems with geometry singularities and natural convection effects. An experimental test was performed in a salt layer of 6.5 m thickness (Charmoille, Daupley, & Laouafa, 2012). This layer is located at about 280 m depth and lies between two layers of clay. The method adopted is direct or reverse injection as depicted in Figure 3(a). The injection time is about 12 days. The inlet flow was $3 \text{ m}^3 \text{ h}^{-1}$ during 4 days followed by $1.5 \text{ m}^3 \text{ h}^{-1}$ during 8 days (Charmoille et al., 2012). Injection was not continuous in time, because there were some stops during a few days due to technical problems.

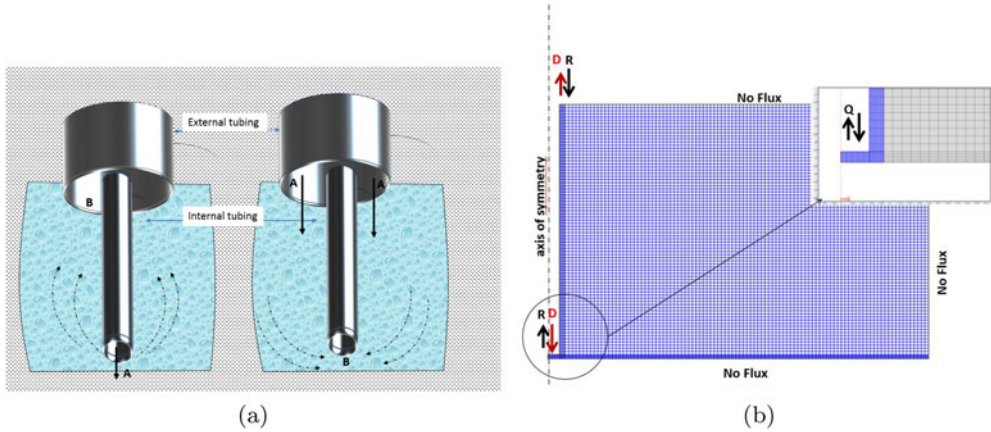


Figure 3. (a) Direct (D) and reverse (R) injection methods; (b) numerical model.

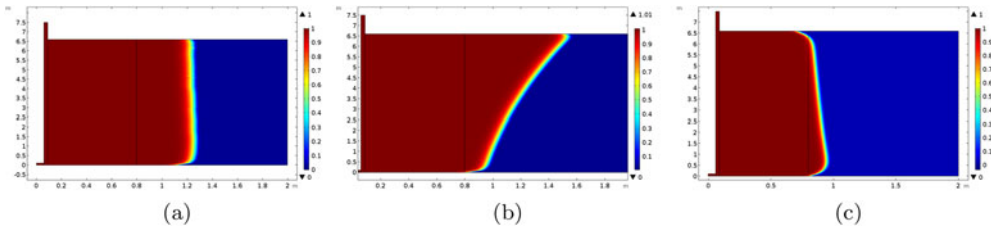


Figure 4. Salt dissolution: Space distribution of porosity after 12 days: Direct method (a), reverse method (b), direct method without gravity (c). Not at scale.

The model assumes axial symmetry. A grid implementation is shown in Figure 3(b). Figure 4 depicts, in the case of a salt formation, the porosity distribution after 12 days using direct or reverse injection method and with or without the gravity term. A porosity equal to one represents the pure fluid cavity.

One can observe that the direction of injection changes the geometrical shape of the cavity with a widening at the top for the case of reverse injection. Figure 5 shows the 3 D shapes of the cavities. After 4 days of injection, the computed dissolved volume is around 12 m^3 , which is very close to the measured *in situ* value around 11 m^3 (Charmoille et al., 2012). After 12 days, the computed dissolved volume is about 38 m^3 and the measured *in situ* is about 40 m^3 .

Figure 6 shows the evolution in time of the cavity in case of direct leaching process, and streamlines and arrows of the normalised fluid velocity. We note a complex spatial distribution of the two fields and also a significant contribution of density effects, mainly present close to the cavity wall.

In the DIM method, the fluid–solid interface is not sharp, but has a certain thickness which depends on the value of the mass exchange coefficient α_i . It is shown in (Luo et al., 2012) that increasing this coefficient leads to thinner dissolving interfaces. Indeed, one obtains mathematically a sharp interface when it tends to infinity. However, intermediate values of α_i must be chosen in order to avoid numerical problems as discussed in Guo et al. (2016). Figure 7 illustrates the position and the evolution of the interface evaluated on a horizontal located at the middle of the model and for different times (a porosity of 1 means liquid and 0 means solid).

The same boundary value problem has been considered but with salt replaced by gypsum rock (Figure 8). We observe in Figure 8, not only a much smaller dissolution rate than in the salt case, but also a significant change in the shape of the cavity. These differences can be easily explained by the contrast of solubility between the two materials, about 360 g L^{-1} for salt and 2.6 g L^{-1} for gypsum. In view of the solubilities and the identical boundary conditions, we could

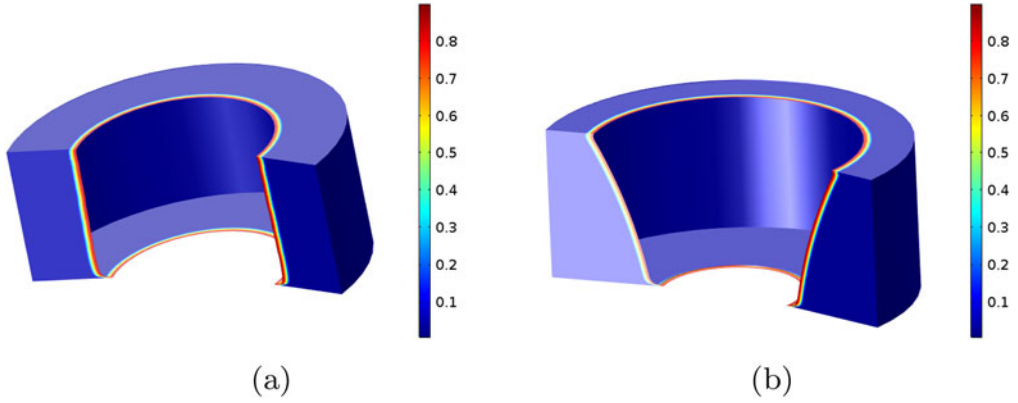


Figure 5. Salt dissolution: 3D view of the cavity obtained after 12 days: Direct method (a) and reverse method (b). Not at scale.

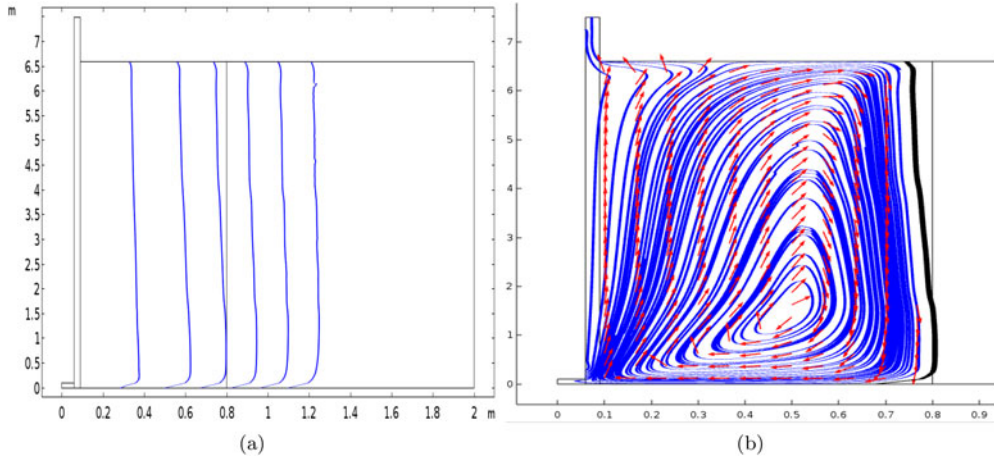


Figure 6. Salt dissolution: Front of the cavity (solid line) every 2 days and (b) example flowlines (solid line) and normalised fluid velocity vectors after 6 days. The horizontal abscissa denotes the distance in m with respect to the axis of symmetry of the model.

have expected, especially in the case where we neglect gravity (for salt) a scale factor between the two cavity sizes on the order of the solubility ratio. More precisely, the expression of the recession velocity for a material (m) is as follows:

$$\mathbf{n}_{sl} \cdot \mathbf{w}_{sl} = \frac{\rho_{lm}}{\rho_{sm}} \frac{1}{(1 - \omega_{eqm})} D_{lm} \mathbf{n}_{sl} \cdot \nabla \Omega_{lm} \quad m = s, g \quad (20)$$

Thus, at the same material point, the ratio between the front recession velocity of gypsum $v_g = \mathbf{n}_{sl} \cdot \mathbf{w}_{sl_g}$ and salt $v_s = \mathbf{n}_{sl} \cdot \mathbf{w}_{sl_s}$ is as follows:

$$\frac{\mathbf{n}_{sl} \cdot \mathbf{w}_{sl_g}}{\mathbf{n}_{sl} \cdot \mathbf{w}_{sl_s}} = \frac{\rho_{ss}}{\rho_{sg}} \times \frac{\rho_{lg}}{\rho_{ls}} \times \frac{(1 - \omega_{eqs})}{(1 - \omega_{eqg})} \times \frac{D_{lg}}{D_{ls}} \times \frac{\mathbf{n}_{sl} \cdot \nabla \Omega_{lg}}{\mathbf{n}_{sl} \cdot \nabla \Omega_{ls}} \quad (21)$$

Densities and diffusion coefficients are not significantly different between the two materials. A rough estimate (assuming same characteristic length-scale) of the flux ratio can be obtained as

$$\frac{\mathbf{n}_{sl} \cdot \nabla \Omega_{lg}}{\mathbf{n}_{sl} \cdot \nabla \Omega_{ls}} \approx \frac{\omega_{eqg}}{\omega_{eqs}} \quad (22)$$

One can see that in Equation (21) the most important factor is the ratio of solubilities. The results show indeed a significant difference between the two actual dissolution rates, but we

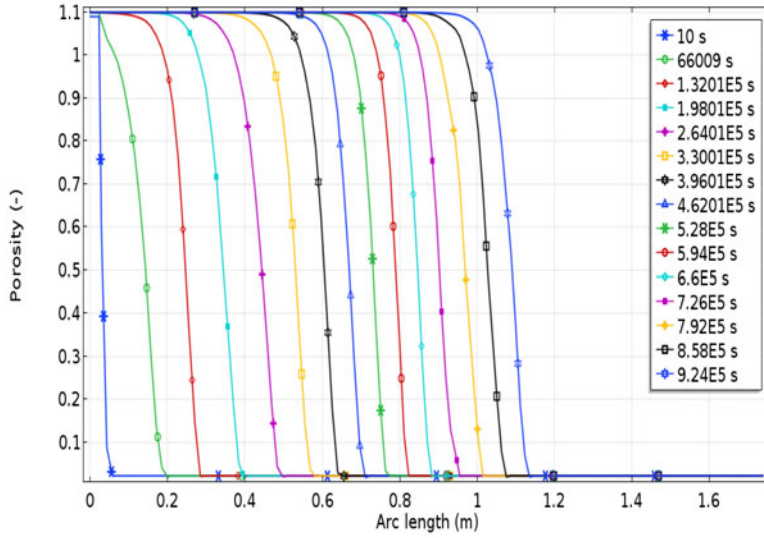


Figure 7. Salt dissolution: Example of porosity distribution along a horizontal line located at the middle of the model and for different times.

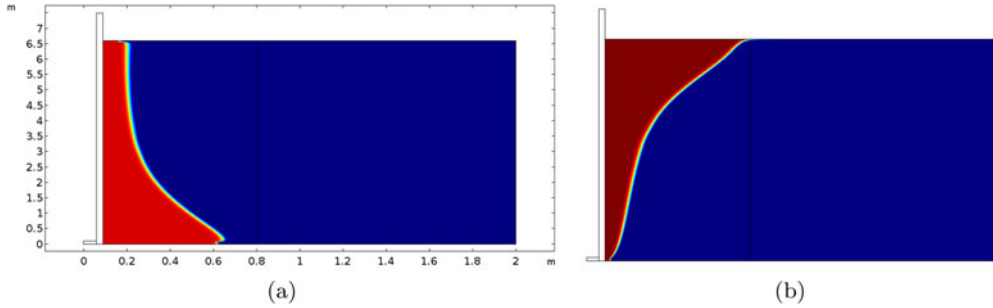


Figure 8. Gypsum dissolution: Space distribution of porosity after 3 years: Direct method (a) and reverse method (b).

also observed a morphological change of the cavity (Figures 4 and 8). Figure 9 illustrates the time evolution of the mean radius for the different conditions and configuration presented above. The mean value in symmetrical axial problems is defined as

$$\bar{r} = \frac{1}{H} \int_S \varepsilon_l(r, z) ds$$

The rate of dissolution τ (unit: [ML⁻²T⁻¹]) at the fluid–solid interface is defined as

$$\tau = \frac{1}{S} \frac{dM}{dt} = \rho_s \mathbf{n}_{sl} \cdot \mathbf{w}_{sl} \quad (23)$$

When dissolution progresses, the fluid/solid interface moves away from the injection point and fluid velocity in the interface vicinity decreases. The reduction of fluid velocity results in a decrease of the dissolution rate. This evolution is not monotonous and is affected potentially by convection cells that come back to the soluble wall.

Figure 10 shows the time evolution of the dissolution rate evaluated at Lines 1, 2 and 3, for various configurations (direct and reverse injection) with or without gravity and for the two rock materials (salt and gypsum). Lines 1, 2 and 3 are located at the bottom, middle and top of the model respectively. Discontinuity in the curves corresponds to the time at which the initial injection is divided by 2.

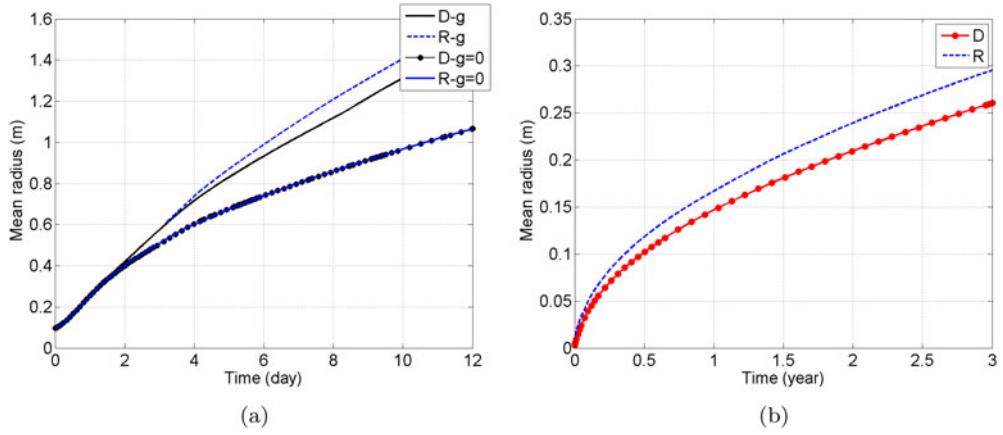


Figure 9. Time evolution of the mean radius \bar{r} for the salt case (a) and for gypsum (b) (D Direct, R Reverse, g gravity).

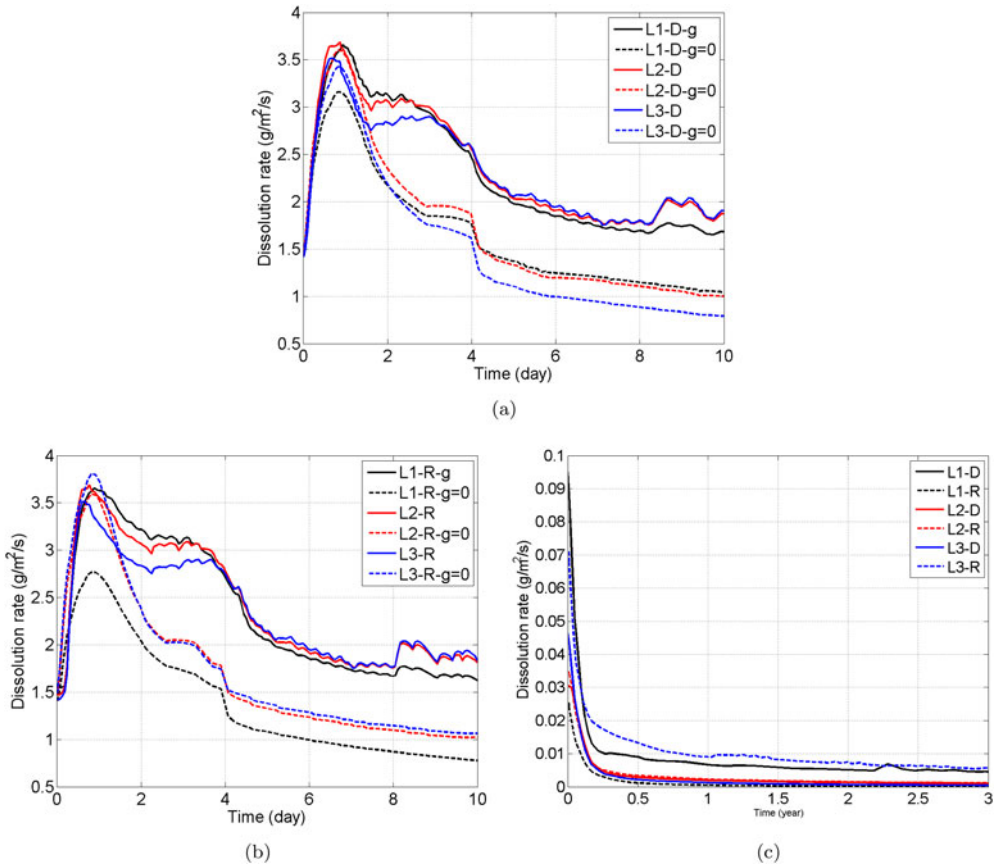


Figure 10. Time evolution of dissolution rate for (a) salt direct injection, (b) salt direct injection and (c) gypsum case. (D Direct, R Reverse, g gravity) (D Direct, R Reverse, g gravity).

In the case of salt, it is observed successively: (i) a non-linear decrease, (ii) a jump associated with the change of the pure water flux injected and (iii) a quasi-linear decrease. The decrease for gypsum dissolution rate is fundamentally different. Decrease is extremely fast. Note, that, as expected, the dissolution rates for the salt and gypsum are different by several orders of magnitude. In these examples, there is a strong non-linear decrease of the rate of dissolution when

the wall deviates from the injection casing. This indicates that the mixed convective component for the transport of chemical species is decreasing rapidly. In this configuration, decrease is slowed down when natural convection vortices are present. One important conclusion of this study is that dissolution may become controlled mainly by density effects (natural convection) if present.

In all cases, we used the DIM implementation. We could have used the ALE method based on [Equation \(9\)](#). It should be noted that the ALE method, which describes explicitly the evolution of the dissolution front through a deforming mesh, faces strong numerical difficulties when the dissolved domain is very large, when there are insoluble bed, layer or zones. In the latter cases, ALE shows difficulties to model dissolution, especially at the corners or any geometrical singularities generated by the dissolution process. Under these conditions, DIM is more robust since the indicator function (here the porosity) is defined on the whole domain and evolves continuously. Singularities are smoothed, although their accurate representation may require a local refinement of the grid [see for instance the application of AMR (adaptive mesh refinement) to dissolution problems in [Luo et al. \(2014\)](#) and [Luo, Laouafa, Debenest, & Quintard \(2015\)](#)].

4. A prospective study of coupling a three-dimensional dissolution modeling with geomechanical issues

In the previous section, we have shown the applicability of the DIM to describe cavity dissolution and have illustrated the kind of information that can be extracted from such models. In this section, we go further by looking at the implications of dissolution on the mechanical stability of the structures involved. The aim of this subsection is not so much to apply the method to real cases but to show the potential application. Therefore, two ‘theoretical’ configurations are considered that are sufficiently representative of real cases.

The first case corresponds to the dissolution of a gypsum pillar in the presence of continuously flowing water. This configuration can be encountered in the case of a room with pillars in a flooded gypsum quarry with a continuous forced convection of fresh water. The second case corresponds to flow induced by a natural hydraulic gradient in a porous rock formation that contains a gypsum lens. This lens is, for instance, located in a porous medium between two layers of marl.

This study is of direct relevance to gypsum mining and natural dissolution of geological formations containing gypsum. Gypsum dissolves easily in flowing water, with time-scales on the order of years (therefore similar to human activity time-scales) as illustrated in [Section 3](#), so that any gypsum mine which becomes flooded on abandonment should be subject to a hydrological and geomechanical study. If a gypsum mine is fully or partially flooded, a continuous saturated or unsaturated flow of fresh water around pillars could decrease significantly their cross sections through dissolution (near the floor level in case of partial flooding) and leads to the pillar failure.

Whatever the hydrogeological configuration, dissolution of gypsum raises the question of consequences in terms of geomechanical behaviour: surface subsidence, sinkholes, caverns or pillar stability, etc. For more information, the reader can refer to the interesting works done by [Parise and Lollino \(2011\)](#), and [Fazio et al. \(2017\)](#). The purpose of this section is to present some examples, indeed simplified, to illustrate the numerical robustness and the potentialities of the numerical dissolution approach outlined in the previous sections.

Here, we are interested in 3D dissolution problems with large spatial scales. Dissolution leads to a time evolution of the domain and boundaries, and changes in the rock matrix porosity and other properties. This in turn leads to rock deformations, which affect the rock properties and thus influences the fluid flow and consequently the dissolution process. An accurate description of this strongly coupled problem must therefore consider the matrix dissolution or evolution and its consequences in terms of modification of the constitutive model for both transport and

mechanics. A model for this strong coupling is currently under development. The mechanical consequences of dissolution are approached in the geomechanical framework proposed in this article through a simplified analysis (weak coupling). For the mechanical response of the rock formation (see Parise & Lollino, 2011 about degradation of the host rock), we only consider the effect of domain change induced by dissolution and fluid pressure on the boundaries. This corresponds to a class of dissolution problems for which flow through the porous formation is sufficiently slow to lead to what is called local equilibrium dissolution characterised by a sharp dissolution front. The dissolution process will generate growing cavities (case of lens) or decreasing cross-section of pillars (case of rooms and pillars in quarries), thus impacting the mechanical response of the formation.

4.1. Three-dimensional modeling of gypsum pillar and gypsum lens dissolution

Figure 11 depicts a cubic gypsum pillar (size $5 \times 5 \times 5$ m) located in a room and pillar quarries. Figure 12 depicts the gypsum lens (size $10 \times 2.5 \times 1.5$ m) located strictly within a porous layer. The injection velocity $V = 10^{-6} \text{ m s}^{-1}$ at the inlet boundary is depicted in Figure 12. The dissolution processes are analysed during 30 years.

We impose no flow conditions at the floor (bottom) and at the roof (top) levels. The modeling parameters are given in Tables 1 and 2.

Figure 13 depicts the pillar state at two different times (15 and 30 years). The left figures give the normalised porosity (blue = 1, red = 0), and the middle height cross section of the pillar every 5 years.

As a result of the different symmetrical properties of the problem (pillar, flow) and low-gradient density effects, symmetry is maintained during the dissolution. Dissolution is naturally more pronounced at the upstream and at the lateral sides of the pillar. Note that the existence of singular corners do not pose significant numerical problems with DIM modeling.

Figure 14 depicts the lens states at three different times (3, 15 and 30 years). We observe the shape evolution of the gypsum lens (in red). The 3D shape of the lens is reconstructed using symmetry. The blue box corresponds to the initial (half) gypsum lens. The dissolution rate of the lens is greater than the pillar dissolution rate. This can be explained, firstly, by the fact that the wet surface is greater for the gypsum lens, and, secondly, by the fact that the ratio of gypsum volume versus reactive surface is smaller for the pillar.

In Figure 15, we show the time evolution of the normalised volume of the pillar and the lens. The dissolution rate for gypsum start to decrease after 20 years, which is due to the fact that the occupation of the porous layer section by the lens starts to decrease after a while, thus allowing for more flow far from the dissolving surface, with, at the same time, a shorter length of the domain in contact with the dissolving material.

The next section is devoted to the study of geomechanical effects induced by such dissolution mechanisms.

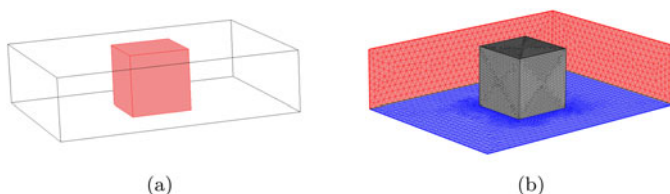


Figure 11. (a) 3D Model of a gypsum pillar (size $5 \times 5 \times 5$ m) located in a flooded gypsum quarry and (b) mesh of the gypsum pillar and the quarry which is subject to a fresh water flow (velocity $V_f = 10^{-6} \text{ m/s}$).

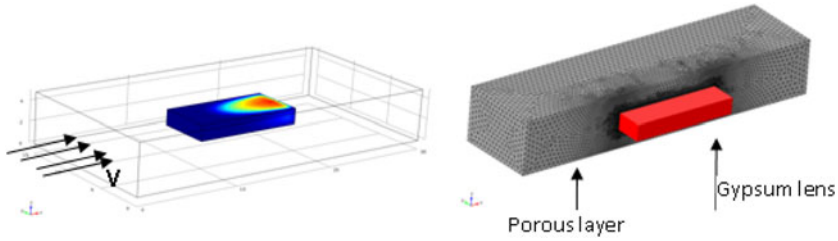


Figure 12. (Left) Lens located in a porous layer. For reasons of symmetry about the vertical midplane, only half model (meshed domain) was considered (right). The mesh corresponds to the investigated domain (field of study). We can also observe the location of the gypsum lens and the porous layer.

Table 1. Mechanical parameters for the pillar and gypsum lens problems.

		E (MPa)	ν []	ϕ (°C)	C (MPa)
Lens	Overburden	4	0.3		
	Porous layer	100	0.3	44	
	Gypsum	35000	0.34	44	8
	Bottom layer	2500	0.3		
Pillar	Gypsum	35000	0.34	44	8
	Room				

Table 2. Geometrical features for the pillar and gypsum lens problems.

Dimensions		Height (m)	Width (m)	Length (m)
Lens	Overburden	10	26	34
	Porous layer	5	26	34
	Gypsum	1.5	10	15
	Bottom layer	5	26	34
Pillar	Gypsum	5	5	5
	Room	5	8	10

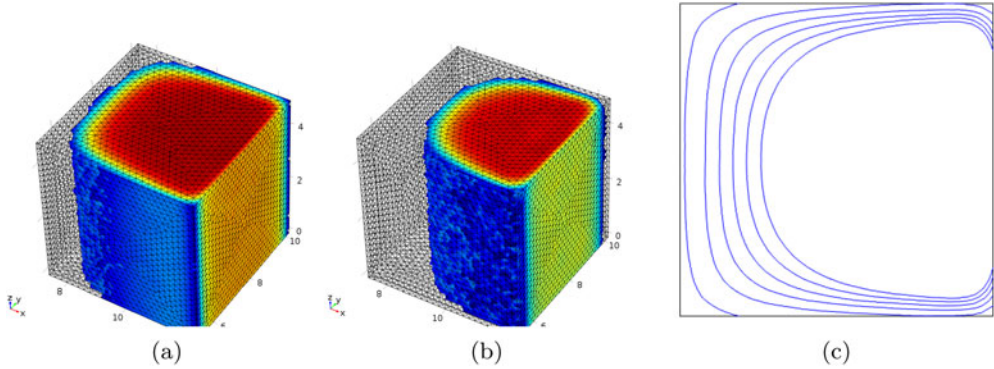


Figure 13. Focus on the pillar shape after (a) 15 years, (b) 30 years and (c) cross section of the pillar every 5 years.

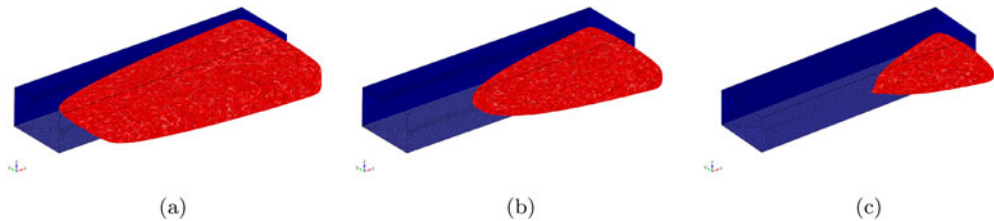


Figure 14. 3D shapes (red) of the lens after (a) 3, (b) 15 and (c) 30 years. The initial volume is represented by the mesh domain.

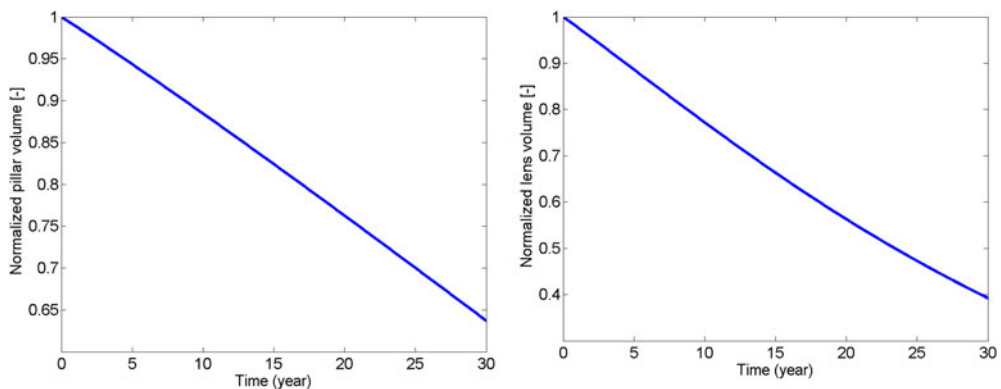


Figure 15. Time evolution of the normalised pillar volume (left) and that of the lens (right).

4.2. Three-dimensional geomechanical modeling of dissolution consequences

The mechanical behaviour of bonded soils or rocks can be described by constitutive models based on the classical theory of hardening plasticity or its extensions. Geomaterial models subject to mechanical and chemical effects are usually presented as chemico-mechanical models or more generally coupled thermal-hydraulic-mechanical-chemical (THMC) models. As a first approach, we use a relatively simple constitutive model in this article. The aim is not so much to describe the geomechanical behaviour precisely but to highlight the potentialities of coupling with the DIM model in order to assess potential geomechanical hazards. This approach is in no way limited by the structure of the constitutive model. In the following, we use a pure and simple mechanical model (elastic-plastic Mohr–Coulomb model). Dissolution being a time continuous process, the mechanical response is also time dependent. In the absence of a numerical tool which integrates the two mechanisms (dissolution and mechanics) with a strong coupling, we used a weak coupling implementation as suggested in the above section.

Two codes, i.e. Comsol (for dissolution) and MSC Marc (for mechanical response), interact with the help of a MATLAB script. The coupling is weak in the sense that there is no mechanical action in the dissolution problem. The algorithm is sequential in time: at a given time step, all data related to the dissolved configuration is transferred to the corresponding mechanical problem.

Gypsum lens

Figure 16 shows the domain containing a gypsum lens. The parameters of the model are given in Tables 1 and 2.

The mechanical consequences of gypsum lens dissolution are illustrated in Figures 17, 18, and 19 for time values equal to $T_i = i \times 30/4$ years.

The first figures give the vertical displacement evolution with time (dissolution). Subsidence increases with dissolution as expected. In some cases, depending on the behaviours of overburden, sinkhole can develop and reach the surface.

Figure 19 gives the value of vertical subsidence along a line located on the surface and passing through the middle of the model, for the four T_i values. Even such small intensity subsidence can affect buildings. In fact this is not so much the intensity of subsidence but its curvature and the position of the structure on the pond which play the major role for the building stability.

Pillar

The second example corresponds to a gypsum pillar loaded on its top by a load $P = 1.875$ MPa (corresponding to an overburden of 70 m width) and located in a gypsum mine. The specific

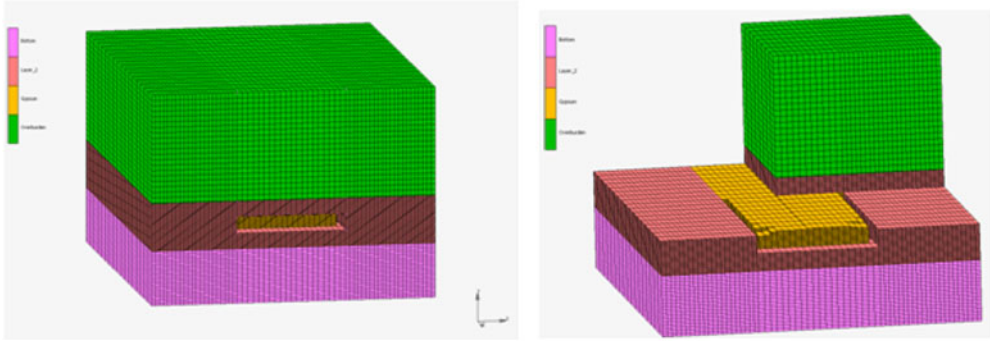


Figure 16. 3D model geomechanical model (left) and location of the gypsum lens (right).

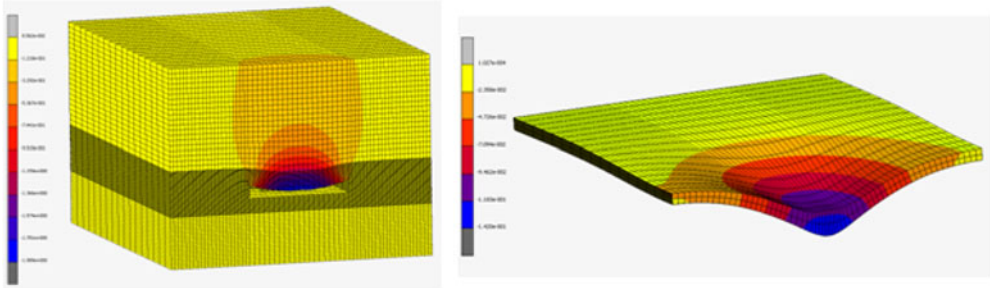


Figure 17. Isovalue of the vertical displacement (left) after the whole dissolution of the gypsum lens, and subsidence pond (right).

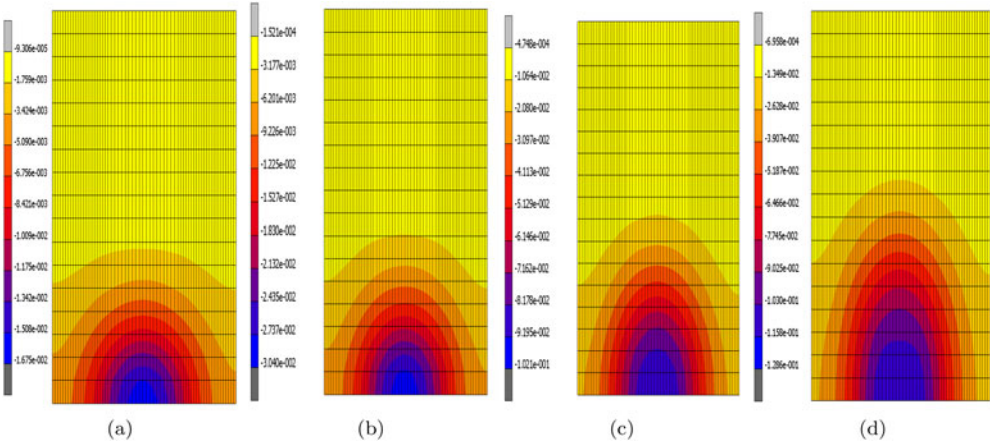


Figure 18. From left to right: top view of surface vertical displacement increasing with four states of dissolution of the gypsum lens.

weight is 2.5 for all material. Figure 20 shows the domain containing the gypsum pillar. The parameters of the model are given in Tables 1 and 2.

In this context, dissolution has the effect of reducing the pillar transversal section. Consequently, it increases the average vertical stress. After a given dissolution period, pillar reaches a critical size and then will no longer support the weight induced by the recovery. Then, we can expect a shearing or buckling if the slenderness of the pillar is too large. Defining the effective plastic strain as follows

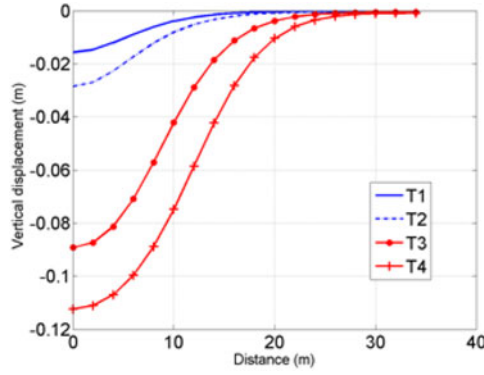


Figure 19. Vertical displacement (subsidence) along a line passing through the middle of the model for four (T1 to T4) states of dissolution.

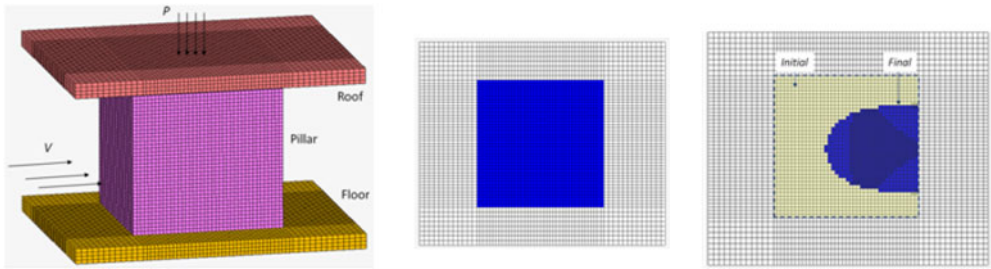


Figure 20. From left to right: Pillar, roof and floor mesh and loading; initial pillar cross section and final pillar cross section.

$$\epsilon_{eq}^p = \int_0^t \dot{\epsilon}_{eq}^p dt \quad \text{with} \quad \dot{\epsilon}_{eq}^p = \sqrt{\frac{2}{3} \dot{\epsilon}_{ij}^p \dot{\epsilon}_{ij}^p}$$

Figures 21 and 22 illustrate a shear pillar failure induced by dissolution. Note that we consider a unique pillar. In the case of several pillars, there would be interactions at the level of the fluid flow and the degree of saturation. Upstream the fluid would be less saturated than downstream. The most rapidly affected pillars would therefore be upstream. Note that stability is performed using limit plastic domain but may be analysed for non-associated material using second-order work criterion (Prunier, Laouafa, & Darve, 2009).

Figure 22 describing the vertical displacement versus increment number shows clearly the corresponding critical (unstable) pillar state.

In our geomechanical modeling, we also used mesh refinement based on the value of effective plastic strain. This explains why the number of element increases and why the shape is not exactly the one coming from dissolution. Figure 22(b) shows the relevance of the developed approach and its predictive feature. Indeed, suppose we know how to determine the critical size of the pillar leading to its collapse. Without a dissolution modeling, there is no information of the moment when this collapse will be effective. The time-dependent coupled dissolution-mechanical (geomechanics) problem allows to perform such a predictive analysis, which is of a crucial importance in the context of risk analysis.

5. Concluding remarks

In this article, we have discussed the problem of the dissolution of rock materials and rock formations, with a focus on salt and gypsum. A modeling approach is developed using a weak coupling (impact of dissolution on mechanical behaviour) between dissolution and geomechanical behaviour. Note that the purpose of this article is to present an approach that can describe the

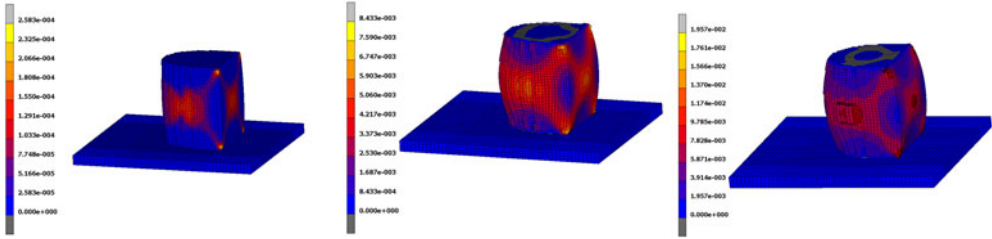


Figure 21. From left to right, examples of the equivalent plastic strain distribution and evolution with dissolution process.

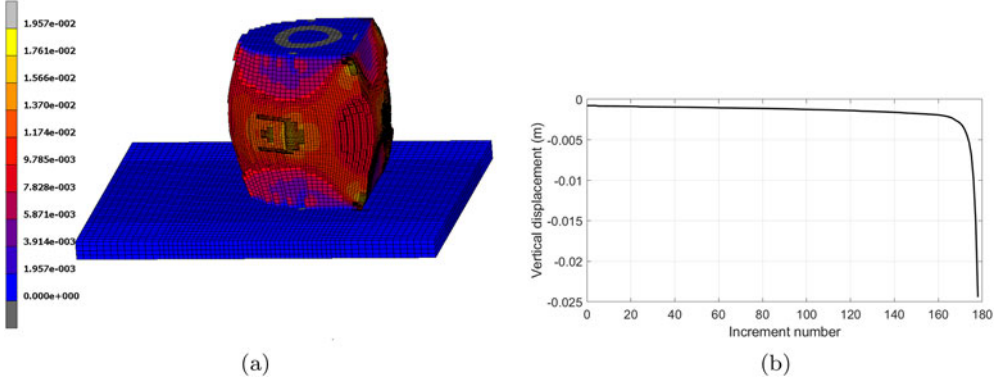


Figure 22. (a) 3D view of the equivalent plastic strain at collapse and (b) time (increment) evolution of the vertical displacement of material at a point located in the center of the roof.

dissolution of solids. The theoretical examples treated in this article and the materials analysed (salt, gypsum) are only for illustration purpose. We underline that the fields of application of the DIM method are very much broader.

The dissolution model is based on a macro-scale or Darcy-scale model obtained by upscaling the microscopic scale or pore-scale equations. The change of scale is based on a volume averaging theory and allows to relate explicitly the form of the macro-scale equations and the effective properties to the pore-scale physics. The application to several problems typically encountered in engineering show:

- the importance of the rock solubility on the cavity formation, with a strong coupling with natural convection for large solubilities and
- the importance of coupling between transport including dissolution and geomechanics.

This weakly coupled sequential approach of dissolution and geomechanics allowed us to obtain already interesting results in terms of risk analysis. Better accuracy, or further applications, would require the introduction of a stronger coupling between geomechanics and dissolution. We expect to integrate in the short term, a strong coupling between dissolution and geomechanics, mainly in the context of leaching. In the case of matrix dissolution, work is under way to describe dissolution of multi-scale heterogeneous media. In such a configuration, the key problem for a relevant coupling is the description of the evolution of the mechanical behaviour of the material. For porous materials, dissolution results in a reduction-modification of the limits of the domain but also into a modification of the pore space. This latter mechanism, depending on its intensity, can radically change the behaviour of the

material (modulus, yield surface, flow rule, etc.) and pose a difficult challenge for the development of a model.

Acknowledgements

J.G. is grateful to the support of the Fundamental Research Funds for the Central Universities.

Disclosure statement

No potential conflict of interest was reported by the authors.

Funding

J.G. was financially supported by the Fundamental Research Funds for the Central Universities [grant number 2682016CX098].

References

- Algive, L., Békri, S., Nader, F. H., Lerat, O., & Vizika, O. (2012). Impact of diagenetic alterations on the petrophysical and multiphase flow properties of carbonate rocks using a reactive pore network modeling approach. *Oil & Gas Science and Technology*, 67(1), 147–160. doi: [10.2516/ogst/2011171](https://doi.org/10.2516/ogst/2011171)
- Békri, S., Renard, S., & Delprat Jannaud, F. (2015). Pore to core scale simulation of the mass transfer with mineral reaction in porous media. *Oil & Gas Science and Technology*, 70(4), 681–693.
- Brenner, H., & Stewartson, K. (1980). Dispersion resulting from flow through spatially periodic porous media. *Philosophical Transactions of the Royal Society A: Mathematical, Physical and Engineering Sciences*, 297(1430), 81–133. doi: [10.1098/rsta.1980.0205](https://doi.org/10.1098/rsta.1980.0205).
- Charmoille, A., Daupley, X., & Laouafa, F. (2012). *Analyse et Modélisation de l'évolution Spatio temporelle des Cavités de Dissolution* (Report No. DRS 12 127199 10107A). INERIS.
- Chen, L., Kang, Q., Carey, B., & Tao, W. (2014). Pore scale study of diffusion reaction processes involving dissolution and precipitation using the lattice Boltzmann method. *International Journal of Heat and Mass Transfer*, 75(0), 483–496. doi: [10.1016/j.ijheatmasstransfer.2014.03.074](https://doi.org/10.1016/j.ijheatmasstransfer.2014.03.074)
- Coutelieres, F. A., Kainourgiakis, M. E., Stubos, A. K., Kikkinides, E. S., & Yortsos, Y. C. (2006). Multiphase mass transport with partitioning and inter phase transport in porous media. *Chemical Engineering Science*, 61(14), 4650–4661. doi: [10.1016/j.ces.2006.02.037](https://doi.org/10.1016/j.ces.2006.02.037)
- De Boever, E., Varloteaux, C., Nader, F. H., Foubert, A., Békri, S., Youssef, S., & Rosenberg, E. (2012). Quantification and prediction of the 3d pore network evolution in carbonate reservoir rocks. *Oil & Gas Science and Technology*, 67(1), 161–178. doi: [10.2516/ogst/2011170](https://doi.org/10.2516/ogst/2011170)
- De Waele, J., Piccini, L., Columbu, A., Madonia, G., Vattano, M., Calligaris, C., ... Forti, P. (2017). Evaporite karst in Italy: A review. *International Journal of Speleology*, 46(2), 137–168. doi: [10.5038/1827_806X.46.2.2107](https://doi.org/10.5038/1827_806X.46.2.2107)
- Donea, J., Giuliani, S., & Halleux, J. (1982). An arbitrary Lagrangian Eulerian finite element method for transient dynamic fluid structure interactions. *Computer Methods in Applied Mechanics and Engineering*, 33(1–3), 689–723. doi: [10.1016/0045_7825\(82\)90128_1](https://doi.org/10.1016/0045_7825(82)90128_1)
- Fazio, N. L., Perrotti, M., Lollino, P., Parise, M., Vattano, M., Madonia, G., & Di Maggio, C. (2017). A three dimensional back analysis of the collapse of an underground cavity in soft rocks. *Engineering Geology*, 238, 301–311. doi: [10.1016/j.enggeo.2017.08.014](https://doi.org/10.1016/j.enggeo.2017.08.014)
- Guo, J., Quintard, M., & Laouafa, F. (2015). Dispersion in porous media with heterogeneous nonlinear reactions. *Transport in Porous Media*, 109(3), 541–570. doi: [10.1007/s11242_015_0535_4](https://doi.org/10.1007/s11242_015_0535_4)
- Guo, J., Laouafa, F., & Quintard, M. (2016). A theoretical and numerical framework for modeling gypsum cavity dissolution. *International Journal for Numerical and Analytical Methods in Geomechanics*, 40(12), 1662–1689. doi: [10.1002/nag.2504](https://doi.org/10.1002/nag.2504)
- Gutierrez, F., Parise, M., De Waele, J., & Jourde, H. (2014). A review on natural and human induced geohazards and impacts in karst. *Earth Science Reviews*, 138, 61–88. doi: [10.1016/j.earscirev.2014.08.002](https://doi.org/10.1016/j.earscirev.2014.08.002)
- Huber, C., Shafei, B., & Parmigiani, A. (2014). A new pore scale model for linear and non linear heterogeneous dissolution and precipitation. *Geochimica et Cosmochimica Acta*, 124, 109–130. doi: [10.1016/j.gca.2013.09.003](https://doi.org/10.1016/j.gca.2013.09.003)
- Jeschke, A. A., Vosbeck, K., & Dreybrodt, W. (2001). Surface controlled dissolution rates of gypsum in aqueous solutions exhibit nonlinear dissolution kinetics. *Geochimica et Cosmochimica Acta*, 65(1), 27–34. doi: [10.1016/S0016_7037\(00\)00510_X](https://doi.org/10.1016/S0016_7037(00)00510_X)

- Jeschke, A. A., & Dreybrodt, W. (2002). Dissolution rates of minerals and their relation to surface morphology. *Geochimica et Cosmochimica Acta*, 66(17), 3055–3062. doi:[10.1016/S0016-7037\(02\)00893-1](https://doi.org/10.1016/S0016-7037(02)00893-1)
- Jourak, A., Hellstrom, J. G. I., Lundstrom, T. S., & Frishfelds, V. (2014). Numerical derivation of dispersion coefficients for flow through three dimensional randomly packed beds of monodisperse spheres. *AIChE Journal*, 60(2), 749–761. doi:[10.1002/aic.14284](https://doi.org/10.1002/aic.14284)
- Kang, Q., Chen, L., Valocchi, A. J., & Viswanathan, H. S. (2014). Pore scale study of dissolution induced changes in permeability and porosity of porous media. *Journal of Hydrology*, 517, 1049–1055. doi:[10.1016/j.jhydrol.2014.06.045](https://doi.org/10.1016/j.jhydrol.2014.06.045)
- Kang, Q., Zhang, D., Chen, S., & He, X. (2002). Lattice Boltzmann simulation of chemical dissolution in porous media. *Physical Review E*, 65(3), 036318.
- Luo, H., Laouafa, F., Debenest, G., & Quintard, M. (2015). Large scale cavity dissolution: From the physical problem to its numerical solution. *European Journal of Mechanics B/Fluids*, 52(Suppl. C), 131–146. doi:[10.1016/j.euromechflu.2015.03.003](https://doi.org/10.1016/j.euromechflu.2015.03.003)
- Luo, H., Laouafa, F., Guo, J., & Quintard, M. (2014). Numerical modeling of three phase dissolution of underground cavities using a diffuse interface model. *International Journal for Numerical and Analytical Methods in Geomechanics*, 38(15), 1600–1616. doi:[10.1002/nag.2274](https://doi.org/10.1002/nag.2274)
- Luo, H., Quintard, M., Debenest, G., & Laouafa, F. (2012). Properties of a diffuse interface model based on a porous medium theory for solid liquid dissolution problems. *Computational Geosciences*, 16(4), 913–932. doi:[10.1007/s10596-012-9295-1](https://doi.org/10.1007/s10596-012-9295-1)
- Martinez, J. D., Johnson, K. S., & Neal, J. T. (1998). Sinkholes in evaporite rocks: Surface subsidence can develop within a matter of days when highly soluble rocks dissolve because of either natural or human causes. *American Scientist*, 86(1), 38–51. doi:[10.1511/1998.1.38](https://doi.org/10.1511/1998.1.38)
- Mauri, R. (1991). Dispersion, convection, and reaction in porous media. *Physics of Fluids A: Fluid Dynamics* (1989–1993), 3(5), 743–756. doi:[10.1063/1.858007](https://doi.org/10.1063/1.858007)
- Nogues, J. P., Fitts, J. P., Celia, M. A., & Peters, C. A. (2013). Permeability evolution due to dissolution and precipitation of carbonates using reactive transport modeling in pore networks. *Water Resources Research*, 49(9), 6006–6021. doi:[10.1002/wrcr.20486](https://doi.org/10.1002/wrcr.20486)
- Olsson, E., Kreiss, G., & Zahedia, S. (2007). A conservative level set method for twophase ow. *Journal of Computational Physics*, 210(1), 225–246.
- Oltéan, C., Golfier, F., & Buès, A. (2013). Numerical and experimental investigation of buoyancy driven dissolution in vertical fracture. *Journal of Geophysical Research: Solid Earth*, 118, 1–11. doi:[10.1002/jgrb.50188](https://doi.org/10.1002/jgrb.50188)
- Osher, S., & Fedkiw, R. P. (2001). Level set methods: An overview and some recent results. *Journal of Computational Physics*, 169(2), 463–502. doi:[10.1006/jcph.2000.6636](https://doi.org/10.1006/jcph.2000.6636)
- Parise, M., & Lollino, P. (2011). A preliminary analysis of failure mechanisms in karst and man made underground caves in Southern Italy. *Geomorphology*, 134(1–2), 132–143. doi:[10.1016/j.geomorph.2011.06.008](https://doi.org/10.1016/j.geomorph.2011.06.008)
- Prunier, F., Laouafa, F., & Darve, F. (2009). 3D bifurcation analysis in geomaterials Investigation of the second order work criterion. *Journal of Environmental and Civil Engineering*, 13(2), 135–147. doi: [10.3166/EJCE13.135-147](https://doi.org/10.3166/EJCE13.135-147).
- Sethian, J. A., & Smereka, P. (2003). Level set methods for fluid interfaces. *Annual Review of Fluid Mechanics*, 35(1), 341–372. doi:[10.1146/annurev.fluid.35.101101.161105](https://doi.org/10.1146/annurev.fluid.35.101101.161105)
- Soulaine, C., Roman, S., Kovscek, A., & Tchelepi, H. A. (2017). Mineral dissolution and wormholing from a pore scale perspective. *Journal of Fluid Mechanics*, 827, 457–483. doi:[10.1017/jfm.2017.499](https://doi.org/10.1017/jfm.2017.499)
- Sun, T. (2012). *Upscaling and multiscale simulation by bridging pore scale and continuum scale models* (PhD thesis). The University of Texas at Austin.
- Szymczak, P., & Ladd, A. J. C. (2004). Microscopic simulations of fracture dissolution. *Geophysical Research Letters*, 31(23), L23606. doi:[10.1029/2004GL021297](https://doi.org/10.1029/2004GL021297)
- Varloteaux, C., Békri, S., & Adler, P. (2013). Pore network modelling to determine the transport properties in presence of a reactive fluid: From pore to reservoir scale. *Advances in Water Resources*, 53(0), 87–100. doi:[10.1016/j.advwatres.2012.10.004](https://doi.org/10.1016/j.advwatres.2012.10.004)
- Varloteaux, C., Vu, M. T., Békri, S., & Adler, P. M. (2013). Reactive transport in porous media: Pore network model approach compared to pore scale model. *Physical Review E*, 87(2), 023010. doi:[10.1103/PhysRevE.87.023010](https://doi.org/10.1103/PhysRevE.87.023010)
- Walters, R. F. (1978). Land subsidence in central Kansas related to salt dissolution. *Kansas University Geological Survey Bulletin*, 214, 82 p.
- Waltham, T., Bell, F., & Culshaw, M. (2005). *Sinkholes and subsidence: Karst and cavernous rocks in engineering and construction*. UK: Praxis Publishing.
- Whitaker, S. (1999). *The method of volume averaging*. Dordrecht, The Netherlands: Kluwer Academic Publishers.
- Zhao, C., Hobbs, B., Ord, A., & Peng, S. (2010). Effects of mineral dissolution ratios on chemical dissolution front instability in fluid saturated porous media. *Transport in Porous Media*, 82(2), 317–335. doi:[10.1007/s11242-009-9427-9](https://doi.org/10.1007/s11242-009-9427-9)

Appendix: Volume averaging of the pore-scale equations

Following the method of volume averaging (Whitaker, 1999), the averages are defined as

$$\Omega_l = \langle \omega_l \rangle^l = \frac{1}{V_l} \int_{V_l} \omega_l dV \quad \text{and} \quad \mathbf{V}_l = \langle \mathbf{v}_l \rangle = \frac{1}{V} \int_{V_l} \mathbf{v}_l dV \quad (\text{A1})$$

where Ω_l represents the intrinsic average of the mass fraction of the dissolving species, V_l the volume of the fluid, V the volume of the REV and \mathbf{V}_l the superficial average of the velocity. The porosity is defined as

$$\varepsilon_l = \frac{1}{V} \int_{V_l} dV. \quad (\text{A2})$$

The pore scale variables can be decomposed by

$$\omega_l = \Omega_l + \omega_l \quad \text{and} \quad \mathbf{v}_l = \varepsilon_l^{-1} \mathbf{V}_l + \mathbf{v}_l \quad (\text{A3})$$

with ω_l and \mathbf{v}_l representing the deviation of the mass fraction of the dissolved species and the liquid velocity, respectively.

The average of the mass balance equations for the liquid and the solid phase gives

$$\frac{\partial \varepsilon_l \rho_l}{\partial t} + \nabla \cdot (\rho_l \mathbf{V}_l) = K_g \quad (\text{A4})$$

$$\frac{\partial \varepsilon_s \rho_s}{\partial t} = K_g \quad (\text{A5})$$

with the mass exchange term expressed as

$$K_g = \frac{1}{V} \int_{A_{ls}} \mathbf{n}_{ls} \cdot \rho_l (\mathbf{v}_l - \mathbf{w}_{sl}) dA = a_{vl} M K_s \left\langle \left(1 - \frac{\omega_l}{\omega_{eq}} \right)^n \right\rangle_{ls} \quad (\text{A6})$$

with $\langle \cdot \rangle_{ls} = \frac{1}{A_{ls}} \int_{A_{ls}} dA$ defined as the surface average and $a_{vl} = \frac{1}{V} \int_{A_{ls}} dA$ as the specific area, respectively.

Considering Equation (A4), the mass balance for the dissolving species gives

$$\varepsilon_l \rho_l \frac{\partial \Omega_l}{\partial t} + \rho_l \mathbf{V}_l \cdot \nabla \Omega_l + \underbrace{\nabla \cdot (\rho_l \langle \omega_l \mathbf{v}_l \rangle)}_{\text{dispersion}} = K_g + K_g \Omega_l + \nabla \cdot \left(\varepsilon_l \rho_l D_l \nabla \Omega_l + \underbrace{\frac{1}{V} \int_{A_{ls}} \mathbf{n}_{ls} \rho_l D_l \omega_l dA}_{\text{tortuosity}} \right). \quad (\text{A7})$$

Based on a bundle of assumptions and transformations, one obtains

$$\begin{aligned} \rho_l \frac{\partial \omega_l}{\partial t} + \rho_l \mathbf{v}_l \cdot \nabla \omega_l + \rho_l \mathbf{V}_l \cdot \nabla \Omega_l - \varepsilon_l^{-1} \nabla \cdot (\rho_l \langle \omega_l \mathbf{v}_l \rangle) - \nabla \cdot (\rho_l D_l \nabla \omega_l) \\ + \frac{\varepsilon_l^{-1}}{V} \int_{A_{ls}} \mathbf{n}_{ls} \cdot \rho_l \omega_l (\mathbf{v}_l - \mathbf{w}_{sl}) dA - \frac{\varepsilon_l^{-1}}{V} \int_{A_{ls}} \mathbf{n}_{ls} \cdot \rho_l D_l \nabla \omega_l dA \\ \rho_l D_l \varepsilon_l^{-1} \frac{1}{V} \int_{A_{ls}} \mathbf{n}_{ls} dA \cdot \nabla \Omega_l \end{aligned} \quad (\text{A8})$$

and the approximation of the nonlinear reaction rate by a first order Taylor's expansion gives

$$\begin{aligned} \mathbf{n}_{ls} \cdot (\rho_l \Omega_l (\mathbf{v}_l - \mathbf{w}_{sl})) + \mathbf{n}_{ls} \cdot (\rho_l \omega_l (\mathbf{v}_l - \mathbf{w}_{sl})) + \mathbf{n}_{ls} \cdot (\rho_l D_l \nabla \omega_l) + \mathbf{n}_{ls} \cdot (\rho_l D_l \nabla \Omega_l) \\ \frac{M K_s}{\omega_{eq}} \left(1 - \frac{\Omega_l}{\omega_{eq}} \right)^{n-1} (\omega_{eq} - \Omega_l - n \omega_l) \quad \text{at } A_{ls} \end{aligned} \quad (\text{A9})$$

Given the mathematical structure of these coupled equations, an approximate solution can be built based on the following form

$$\omega_l = s_l (\Omega_l - \omega_{eq}) + \mathbf{b}_l \cdot \nabla \Omega_l + \dots \quad (\text{A10})$$

where s_l and \mathbf{b}_l are called closure variables.

Substituting the above two equations into Equation (A8) leads to the closed form of the mass balance of the dissolved species

$$\frac{\partial \varepsilon_l \rho_l \Omega_l}{\partial t} + \nabla \cdot (\rho_l \Omega_l \mathbf{V}_l + \varepsilon_l \rho_l (\Omega_l - \omega_{eq}) \mathbf{U}_l^*) - \nabla \cdot (\varepsilon_l \rho_l \mathbf{D}_l^* \cdot \nabla \Omega_l) = K_g \quad (\text{A11})$$

with the dispersion tensor and the non traditional effective velocity given by

$$\mathbf{D}_l = D_l \left(\mathbf{I} + \frac{1}{V_l} \int_{A_{ls}} \mathbf{n}_{ls} \mathbf{b}_l dA \right) \cdot \langle \mathbf{v}_l \mathbf{b}_l \rangle^l \quad (\text{A12})$$

and

$$\mathbf{U}_I^* = \langle \mathbf{v}_I s_I \rangle^I = \frac{1}{V_I} \int_{A_{Is}} \mathbf{n}_{Is} D_I s_I dA \quad (\text{A13})$$

respectively. The mass exchange term is given by

$$K_g = a_{VI} M \left(1 - \frac{\Omega_I}{\omega_{eq}} \right)^n k_{s,eff} + a_{VI} M \left(1 - \frac{\Omega_I}{\omega_{eq}} \right)^{n-1} \mathbf{h}_I^* \cdot \nabla \Omega_I \quad (\text{A14})$$

where the effective reaction rate coefficient and the additional gradient term coefficient in Equation (A14) are defined as

$$k_{s,eff} = k_s (1 + n \langle s_I \rangle_{Is}) \quad (\text{A15})$$

and

$$\mathbf{h}_I^* = n \frac{k_s}{\omega_{eq}} \langle \mathbf{b}_I \rangle_{Is} \quad (\text{A16})$$

It is noteworthy that Equation (A14) is recovered when considering kinetic boundary conditions at the solid liquid interface, i.e. Equation (5). If a thermodynamic equilibrium condition $\omega_I = \omega_{eq}$ is prescribed, the corresponding mass exchange term can be rewritten as

$$K_g = \rho_I \alpha_I (\Omega_I - \omega_{eq}) + \rho_I \mathbf{h}_I \cdot \nabla \Omega_I \quad (\text{A17})$$

where the following notations for the mass exchange coefficient

$$\alpha_I = \frac{1}{V} \int_{A_{Is}} \mathbf{n}_{Is} \cdot (D_I \nabla s_I) dA \quad (\text{A18})$$

and the additional gradient term

$$\mathbf{h}_I = \left(\frac{1}{V} \int_{A_{Is}} \mathbf{n}_{Is} \cdot (D_I \nabla \mathbf{b}_I) dA \right) \quad (\text{A19})$$

have been adopted.

All the above effective parameters can be obtained by solving the two closure problems as presented in (Guo et al., 2015). One must remember that the macro scale problem should be completed with the following averaged equations

$$\frac{\partial \varepsilon_I \rho_I}{\partial t} + \nabla \cdot (\rho_I \mathbf{V}_I) = K_g \quad \text{and} \quad \frac{\partial \varepsilon_S \rho_S}{\partial t} = K_g \quad (\text{A20})$$